Applied Thermal Engineering 258 (2025) 124746

Contents lists available at ScienceDirect

Applied Thermal Engineering

journal homepage: www.elsevier.com/locate/apthermeng

Research Paper

Self-powered wireless sensor networks based on the radioisotope thermoelectric generator for aquatic temperature monitoring

Chao Chen [a,1], Chen Wang [a,1], Zhiheng Xu [a,b,*], Mingxin Bian [a], Hongyang Jia [a], Ting Cai [a], Yunpeng Liu [a,b], Xiaobin Tang [a,b,*]

[a] Department of Nuclear Science and Technology, Nanjing University of Aeronautics and Astronautics, Nanjing 210016, China
[b] Key Laboratory of Nuclear Technology Application and Radiation Protection in Aerospace, Ministry of Industry and Information Technology, Nanjing 211106, China

ARTICLE INFO

Keywords:
Aquatic temperature monitoring
Wireless sensor networks
Radioisotope thermoelectric generator
Underwater
Stability

ABSTRACT

This study focuses on the development of ultra-long-life wireless sensor network (WSN) node based on the thermoelectric effect for use in areas such as aquatic temperature monitoring. A long-lasting radioisotope thermoelectric generator (RTG) was used as the energy source for the WSN node to address issues such as short runtime and pollution associated with traditional chemical batteries and solar cells. A compact RTG was fabricated by developing thermoelectric modules with high adaptability to cylindrical heat sources. The electrical output performance at the ocean surface and in the underwater environment was analyzed, with the maximum output power reaching 2326.6 μW. An integrated circuit module comprising direct current to direct current (DC-DC) boost converters, control switch circuits, and supercapacitors was employed to power the WSN node from the RTG directly. Powered by the RTG, a WSN node for monitoring ocean temperature was also constructed. Its performance was evaluated under different environmental conditions by investigating the effects of RTG's output, sensor data variations, distance, and other factors on WSN node stability. Results demonstrate that the designed self-powered WSN node can operate stably and continuously at the ocean surface and in underwater environments, thereby showing its promising prospects.

1. Introduction

As greenhouse gas emissions continue to rise, the oceans are facing the unprecedented challenges of temperature increase[1]. The rising ocean temperatures have profound impacts on climate[2], exacerbating global warming trends[3] and altering the heat exchange dynamics between land and ocean[4]. These outcomes induce climate change on a global scale[5]. Hence, the continuous monitoring of aquatic temperature is imperative. Wireless sensor networks (WSNs) are rapidly emerging and developing; for instance, they are applied in various fields, such as quality monitoring[6], precision agriculture[7], smart industries applications[8], military[9], and civilian domains[10,11]. Ocean observation buoy systems can monitor ocean surface temperature or humidity in real time by utilizing WSNs[12]; thus, WSNs play a crucial role in the real-time observation of oceanic climate and hydrological environment changes[13]. Comprising numerous sensor nodes, WSNs are well-suited for large-scale monitoring of the seawater temperature. Currently, individual WSN nodes are typically powered by chemical batteries, solar cells, or wind power generation, as shown in Fig. 1 [14,15]. Although WSN operation requires no human intervention, chemical batteries are prone to leakage, causing pollution; thus, significant manpower is wasted on battery replacement and installation when battery levels are low[16]. Solar cells are viable only under abundant sunlight conditions; thus, similar to chemical batteries, solar cells are confronted with significant limitations[17,18]. Thus, the development of a long-life stable power supply system suitable for WSN nodes is imperative to address the issue mentioned and realize the establishment and long-term operation of ocean temperature monitoring systems based on WSN nodes. Radioisotope thermoelectric generators (RTGs), characterized by long service life[19], high stability[20], and minimal susceptibility to environmental influences[21], have emerged as promising candidates for WSN node power systems.

RTGs generate electricity based on the Seebeck effect[22]. They can

Abbreviations: WSN, Wireless sensor network; RTG, Radioisotope thermoelectric generator; TE, Thermoelectric; DC-DC, Direct current to direct current; V–I, Voltage-current; P–I, Power-current.

* Corresponding authors at: Department of Nuclear Science and Technology, Nanjing University of Aeronautics and Astronautics, Nanjing 211106, China.
E-mail addresses: xuzhiheng@nuaa.edu.cn (Z. Xu), tangxiaobin@nuaa.edu.cn (X. Tang).

[1] These authors contributed equally to this work and should be considered co-first authors.

https://doi.org/10.1016/j.applthermaleng.2024.124746
Received 16 June 2024; Received in revised form 26 September 2024; Accepted 28 October 2024
Available online 29 October 2024
1359-4311/

Nomenclature

Φ	Power density of the heat source, W/cm^3
T	Temperature, K
α	Thermal diffusivity, mm^2/s
ρ	Density of the heat source, g/cm^3
C	Specific heat capacity, J/(K·g)
Q_h	Heat flux into the hot side of the thermoelectric module, J
S_N	Seebeck coefficient of P-type thermoelectric leg, V/K
S_P	Seebeck coefficient of N-type thermoelectric leg, V/K
T_c	Cold side temperature, K
T_h	Hot side temperature, K
k	Thermal conductivity, W/(m·K)
k_P	Thermal conductivity of P-type thermoelectric material, W/(m·K)
k_N	Thermal conductivity of P-type thermoelectric material, W/(m·K)
A_P	Cross-sectional area of P-type thermoelectric leg, mm^2
A_N	Cross-sectional area of N-type thermoelectric leg, mm^2
l_P	Length of P-type thermoelectric leg, mm
l_N	Length of N-type thermoelectric leg, mm
ρ_P	Resistivity of P-type thermoelectric leg, Ω/m
ρ_N	Resistivity of N-type thermoelectric leg, Ω/m
R_{in}	Internal resistance of RTG, Ω
R_L	External load resistance in the RTG, Ω
V	Output voltage of the RTG, V
V_{oc}	Open-circuit voltage of the RTG, V
I	Output current of the RTG, A
I_{sc}	Short-circuit current of the RTG, A
P_{out}	Output power of the RTG, W
P_{max}	Maximum output power of the RTG, W

directly convert decay heat from isotopes into electrical energy[23]. Currently, RTGs are mostly used in several cubic meters or even larger to achieve high outputs. However, WSN nodes often have relatively small volumes because of the large number of deployments, making the matching between RTGs and WSN nodes crucial. Researchers have made significant efforts for the miniaturization and performance enhancement of RTGs[24,25]. For example, Liu et al. [26] synthesized two small-scale RTGs that can obtain a maximum open-circuit voltage of 1.56 V and a maximum output power of 3.39 mW at 398.15 K. Yuan et al. [27] made the micro-RTG through stacking integration at a temperature difference of 48 K, voltage density of 2.21 V cm^{-3}, and power density of 514.25 μW cm^{-3}. Bian et al. [28] fabricated thermoelectric (TE) modules with different shapes by using direct-writing 3D printing technology; these modules can produce a maximum output power of 2.28 mW. However, in these studies, the output power of RTGs typically remains in the milliwatt range, whereas the power consumption of sensors used in WSNs is mostly in the watt range[29]. As a result, directly powering the sensor components by using the small-scale RTG is challenging[30].

In this work, a TE module with high adaptability to isotopic heat sources is designed and fabricated. Given the limitations in the electrical output performance of the small-volume RTG, a specialized energy harvesting circuit tailored for RTG was designed. This circuit was configured with direct current to direct current (DC-DC) converters, supercapacitors, and control switch circuits to boost effectively and

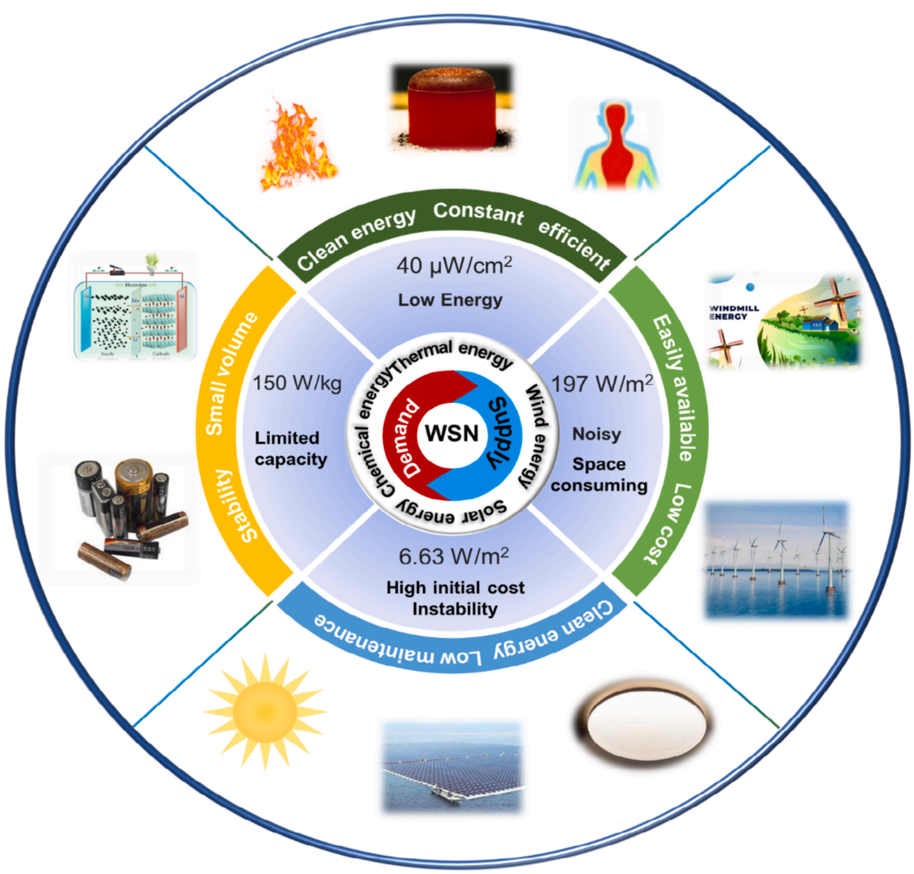

Fig. 1. Applications of WSN with different energy sources.

manage precisely the micro-electrical energy generated by the RTG, thereby ensuring maximal energy collection efficiency and utilization efficiency. Subsequently, a WSN node system was realized by integrating the RTG, energy harvesting circuit, and a temperature-sensor component. This system can enable a stable power supply to the sensor components through the RTG. The research findings provide new insights into WSN power supply and expand the application domains of RTGs.

2. Materials and methods

2.1. Preparation and measurements of RTG

RTG is primarily composed of isotopic heat sources and TE modules [31]. However, researchers in the field of radiation heat–type isotope batteries often use electrically heated equivalent sources as radioactive isotopic heat sources to conduct various performance tests and analytical studies because of the expensive cost, scarce availability, and high toxicity of isotopic heat sources. In this study, alumina electric heater pipes were used to replace $^{238}PuO_2$ and $^{90}SrTiO_3$ isotopic heat source cores, and the graphite with high thermal conductivity was employed as the casing for the isotopic heat source. The graphite casing of the designed heat source and heater pipes are illustrated in Fig. 2. The corresponding geometric parameters are listed in Table 1.

The heat harvesting and electrical energy conversion component in the system are comprised of four Bi_2Te_3-based TE modules connected in series with flexible electrodes, as shown in Fig. 3. Table 2 lists the parameters of the individual TE modules, with an electrode length of 7 mm between the modules.

2.2. Control equation for RTG

The transfer of energy in the radioisotope heat source and the TE module is shown in the Fig. 4. And the flow of heat conforms to the three-dimensional Fourier's law of heat conduction[32].

$$\frac{\Phi}{\rho C} = \frac{\partial T(t,x,y,z)}{\partial t} - \alpha \Delta T \tag{1}$$

where Φ represents the power density of the heat source; T is temperature; α denotes thermal diffusivity; ρ represents the density of the heat source; C denotes specific heat capacity.

As represented in Fig. 4, the TE module is composed of multiple P-type and N-type TE legs interconnected via metal conductors, configured in a thermal parallel and electrical series arrangement. Ceramic plates are employed above and below as thermal conductive and insulating materials. The heat transfer from the radioisotope heat source to the hot end of the TE module is denoted as Q_h, which can be expressed as[33]:

$$Q_h = (\overline{S_P} - \overline{S_N})T_h I + k(T_h - T_c) - \frac{1}{2}I^2 R_{in} \tag{2}$$

Table 1
Parameters of the components included in the equivalent heat source.

Component	Graphite Housing	Heater Pipe
Parameter	Semidiameter: 25 mm Height: 60 mm Internal hole semidiameter: 6 mm Internal hole height: 45 mm	Semidiameter: 3 mm Height: 20 mm Working limit: 24 V/50 W

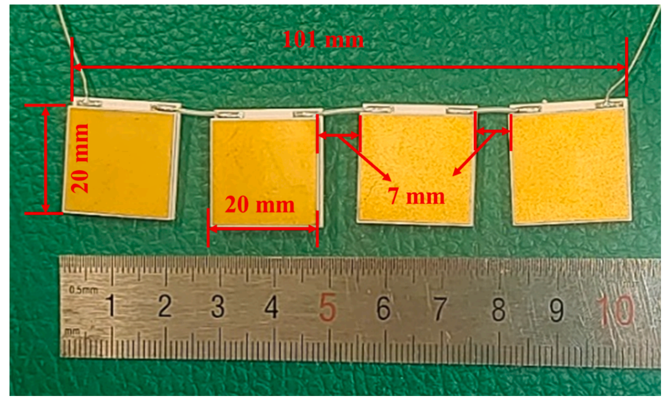

Fig. 3. Four Bi_2Te_3-based TE modules.

Table 2
Parameters of the components included in the equivalent heat source.

TE Module	Parameter
Size/mm × mm × mm	20 × 20 × 2.87
Number of component leg pairs	32
Thickness of the ceramic substrate/mm	0.64
Thickness of the coating/mm	0.14
Size of TE leg/mm × mm × mm	1.4 × 1.4 × 1.25
N-type TE material	$Bi_2Te_{2.97}Se_{0.03}$
P-type TE material	$Bi_{0.5}Sb_{1.5}Te_3$

where S_P and S_N represent the Seebeck coefficients of the P-type and N-type TE materials, respectively; k and R_{in} denote the thermal conductivity and internal resistance of the TE module, respectively, as follows [34]:

$$k = \frac{k_P A_P}{l_P} + \frac{k_N A_N}{l_N} \tag{3}$$

$$R_{in} = n \cdot \left(\frac{\rho_P l_P}{A_P} + \frac{\rho_N l_N}{A_N} \right) \tag{4}$$

where n represents the number of TE couples; k_P and k_N represent the the

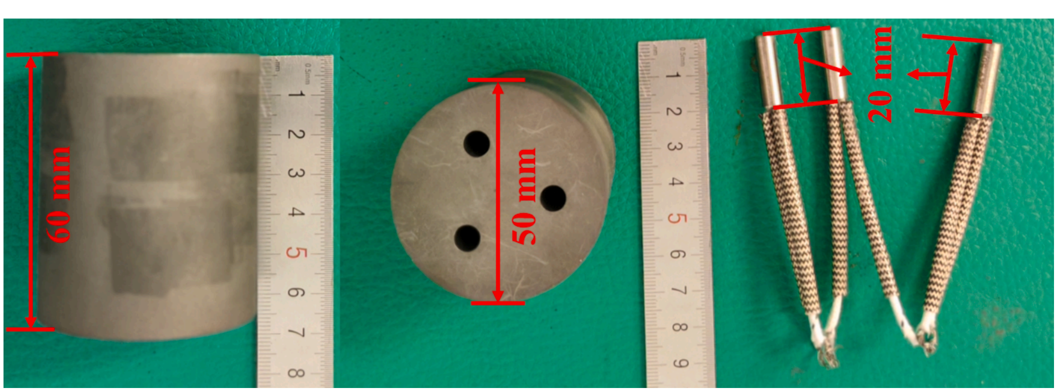

Fig. 2. Graphite casing and heater pipes of the designed heat source.

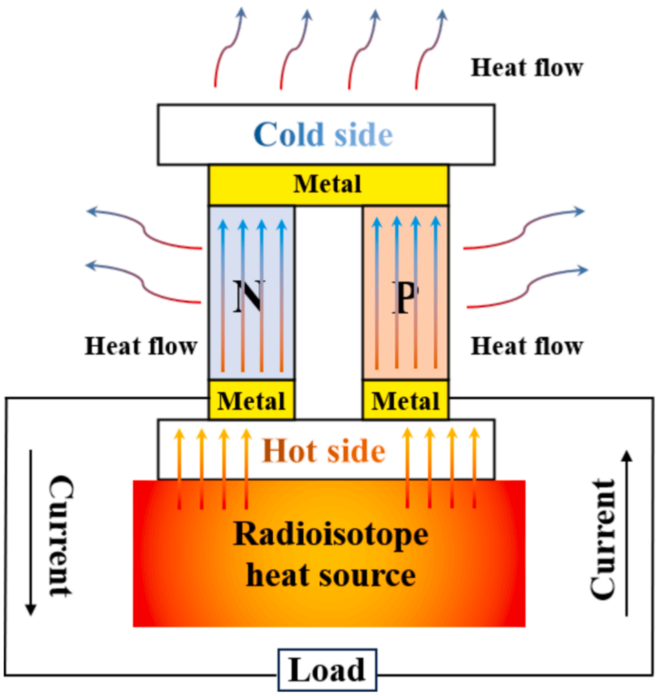

Fig. 4. Energy flow in the radioisotope heat source and the TE module.

thermal conductivity of the P-type and N-type TE materials; A_P and A_N represent the Cross-sectional area of the P-type and N-type thermoelectric leg; l_P and l_N represent the length of the P-type and N-type thermoelectric leg; ρ_P and ρ_N represent the resistivity of P-type thermoelectric leg, respectively.

At the thermal equilibrium, the generated Seebeck voltage (the open-circuit voltage) can be determined as follows:

$$V_{oc} = n\cdot(S_P - S_N)\cdot(T_h - T_c) \tag{5}$$

Following the connection of the external load resistance, the current and the output power can also be indicated as

$$I = \frac{n\cdot(S_P - S_N)\cdot(T_h - T_c)}{R_L + R_{in}} \tag{6}$$

$$P_{out} = \frac{n^2\cdot(S_P - S_N)^2\cdot(T_h - T_c)^2}{R_{in} + R_L} \tag{7}$$

When the load resistance is equal to the internal resistance of the TE module ($R_{in} = R_L$), the maximum output power is given by

$$P_{\max} = \frac{n^2\cdot(S_P - S_N)^2\cdot(T_h - T_c)^2}{4R_{in}} \tag{8}$$

2.3. Composition of the WSN node

The self-assembled WSN node system consists of three components: RTG, energy management circuit, and temperature sensor. RTG comprises an isotopic heat source and TE modules. The isotopic heat source serves as the primary energy source for the system, and the TE module functions as the component for converting thermal energy into electrical energy. Small-scale RTGs employed in the WSN encounter limitations due to the compact size of their internal TE modules, resulting in a reduced temperature differential between the hot and cold ends that quickly stabilizes. As a result, sufficient output voltage and power for sustaining the WSN node operation cannot be generated. Consequently, appropriate energy-harvesting circuits, which can effectively harness the weak electrical energy generated by isotopic TE generators to power wireless sensors for real-time ocean temperature monitoring, are designed for the RTG, as shown in Fig. 5. Fig. 5(a) shows the temperature sensor receiver side of the WSN node. The transmitter side mainly consists of DC-DC boost converters, a control switch model, and a temperature sensor transmitter with the interface for supercapacitor and RTG, as shown in Fig. 5(b). The DC-DC boost converter elevates the low output voltage of the RTG to a level capable of driving the WSN node. The supercapacitor is utilized for storing the electrical energy generated by the RTG. The temperature sensor transmitter is also integrated. The control switch model is employed to manage the transition between energy storage and release by comparing the supercapacitor voltage with the set voltage of 2.9 V and 3.6 V. When charging until the voltage of the supercapacitor reaches 3.6 V, the temperature sensor starts to work, and stops working after decreasing to 2.9 V, then continues to charge, and so on. The utilization of the designed energy harvesting circuit enables the self-powering of WSN nodes without the need for additional external power sources. And more detailed information on circuit design is shown in Figs. S1, S2, and S3 of the Supplementary Material.

2.4. Experimental conditions and instruments

The surface temperature of the heat source and the underwater environment temperature at different power levels were measured using a multichannel temperature measurement instrument and an infrared thermal imaging camera. The power of the heat source was adjusted by a DC power supply, which can supply a maximum power of 150 W. The output performance of the RTG was measured by the parameter analyzer (Keithley 4200 SCS). A data acquisition card (DAM-3158A) was used to monitor the real-time output voltage of the RTG and supercapacitor during the operation of WSN node.

3. Results and discussion

3.1. Output performance of RTG based on the columnar heat source

TE modules were mounted onto the designed heat source to test the output performance of the designed RTG applied to ocean temperature monitoring. High temperature–resistant polyimide tape was used to bind the TE modules to the heat source to prevent detachment. The heat source power was set within the 5–15 W range. The results of surface temperature distribution are shown in Fig. S4 in the Supplementary Material. Different temperatures could be achieved on the heat source surface by adjusting the power applied to the heater pipe. The heat source temperature steadily increased with increasing heat power, and the temperature gradually decreased from the inside to the outside. This phenomenon was caused by heat diffusion. The surface temperature differentials of the cylindrical heat source were smaller than those of the flat heat source[34] under similar surface temperature conditions. This finding reflects the compact structure and uniform surface temperature distribution characteristics of the cylindrical heat source. Unlike the previous works, this study fabricated an equivalent cylindrical heat source suitable for RTG. And its operational life span when applied to the WSN node was evaluated as shown in Figs. S5 and S6 in the Supplementary Material. The results show that $^{238}PuO_2$ and $^{90}SrTiO_3$ radioisotope heat sources can sustain effective operation for decades.

Two environmental settings were compared in the tests of RTG: the ocean surface and the underwater environment. At the ocean surface, the RTG was cooled by natural convection. In the underwater environment, a water-cooling device was used to prevent the temperature of water from rising too quickly. The actual test scenarios and the test results of RTG output performance in different environments are shown in Fig. 6. As the heat source power increases, the temperature difference across the TE module gradually increases, leading to an improvement in the output performance of the RTG in the two environments. The I–V/P–I curves of the RTG operating at the ocean surface are shown in Fig. 6 (a). When the equivalent heat source power is 15 W, the RTG achieves

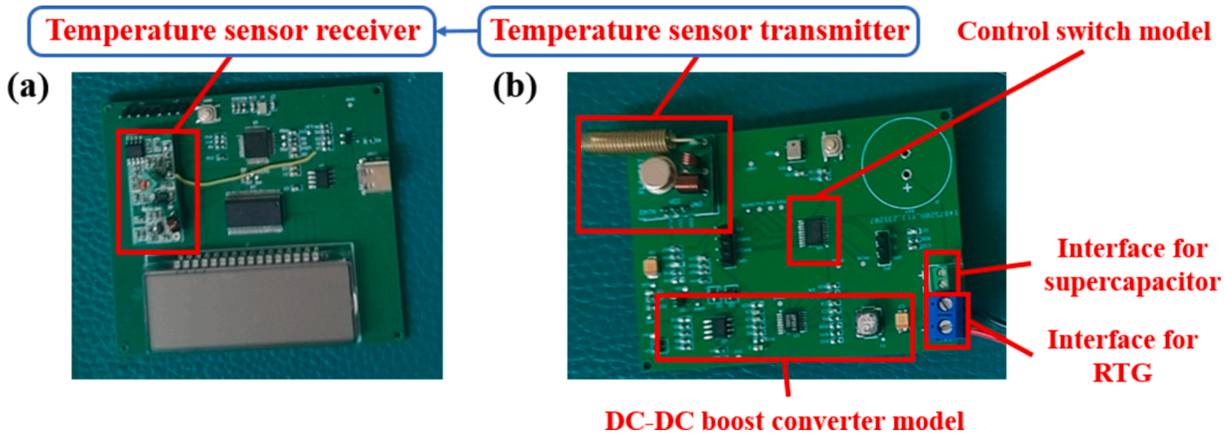

Fig. 5. Integrated circuit module for WSN node (a) receiver and (b) transmitter.

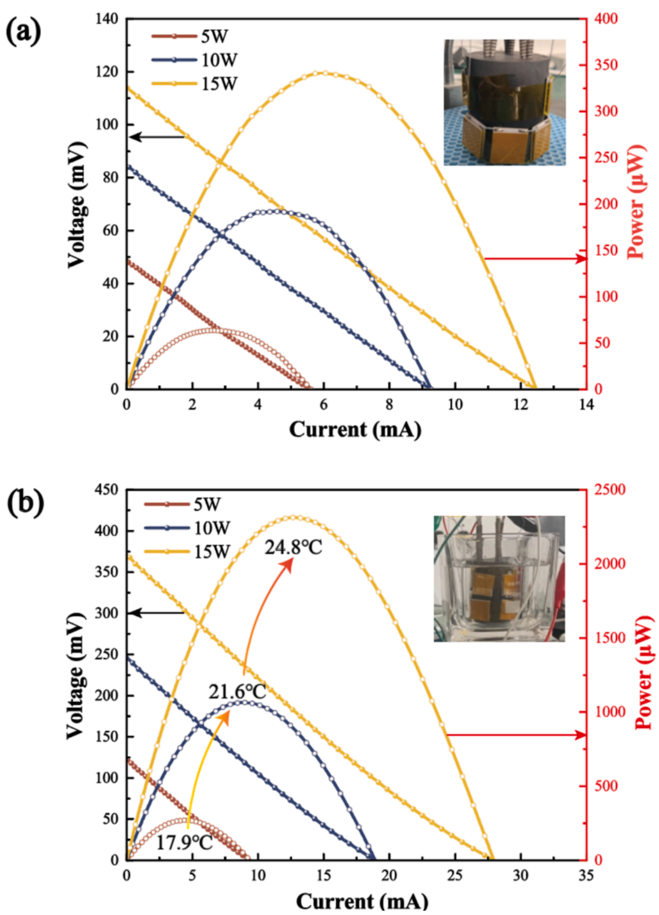

Fig. 6. Output performance of RTG (a) at the ocean surface and (b) in the underwater environment.

P_{max} of 341.3 μW, V_{oc} of 113.8 mV, and I_{sc} of 12.6 mA.

The output performance of the RTG operating in the underwater environment is shown in Fig. 6(b). When the equivalent heat source power is 15 W, the RTG achieves P_{max} of 2326.6 μW, V_{oc} of 376 mV, and I_{sc} of 28.2 mA. Regardless of the heat source power, the output of the RTG in the underwater environment is higher than that at the ocean surface. This finding indicates that the underwater environment has a positive influence on the output performance of RTG. When the heat source power is increased from 5 W to 15 W, the maximum output power of the RTG at the ocean surface increases by 435.79 %. Moreover, the maximum output power of RTG in underwater environments has increased by 759.79 %, much higher than on the ocean surface. This finding indicates that as the heat source power increases, the positive gain in the RTG output performance from the underwater environment becomes more significant than that from the ocean surface.

The influence of the heat source on the water temperature is significant during the equivalent experiment because of the small capacity of the beakers used in the experiment. Therefore, the water temperature was monitored when it reached a steady state at different heat source powers. As the heat source power increases, the water temperature rises significantly. However, the ocean experiences little to no temperature rise in real-world conditions. Therefore, the output performance of the RTG in actual underwater environments may be even better than experimentally observed.

3.2. Testing of the WSN node operational state

Together with the energy management circuit and supercapacitor, the RTG serves as the power source, and the wireless temperature sensor functions as the load in the assembled self-powered WSN node. The operational state of the node when applied to ocean temperature monitoring was tested to assess its performance. The test results are shown in Fig. 7. The thermal power of the RTG was set to 10 W. Two TE modules were connected in series in the RTG to ensure the proper operation of the DC-DC boost converter, and a 0.1F supercapacitor was used as the energy storage device. The output voltage of the RTG, the stored energy of the supercapacitor (voltage at the ends of the supercapacitor), and the ambient air temperature data monitored by the sensor were recorded in real time. Fig. 7(a) shows the test results of the system operating at the ocean surface. The WSN node started collecting from the voltage of 2 V, and two duty cycles in 59.8 min were completed. The duration of energy collection before the sensor starts working is 40.6 min. At this time, the voltage generated by the RTG ranged from 70 mV to 90 mV, with an average output voltage of 80 mV. The initial fluctuations in the RTG output voltage may be attributed to subtle air circulation in the environment.

The test results for operation in the underwater environment are shown in Fig. 7(b). The voltage generated by the RTG ranges from 67 mV to 87 mV, with an average output voltage of 82 mV. The total time consumed for two cycles is 47.1 min. The energy collection time in the underwater environment before the sensor starts working is 27.9 min, which is significantly shorter than that in the ocean surface environment. Water flow cools the TE module better than air convection at the ocean surface, thereby increasing the temperature difference between the two ends of the TE module. This scenario results in a high output power of the RTG, which speeds up the system's charging process. Additionally, the use of RTG in the underwater environment results in a

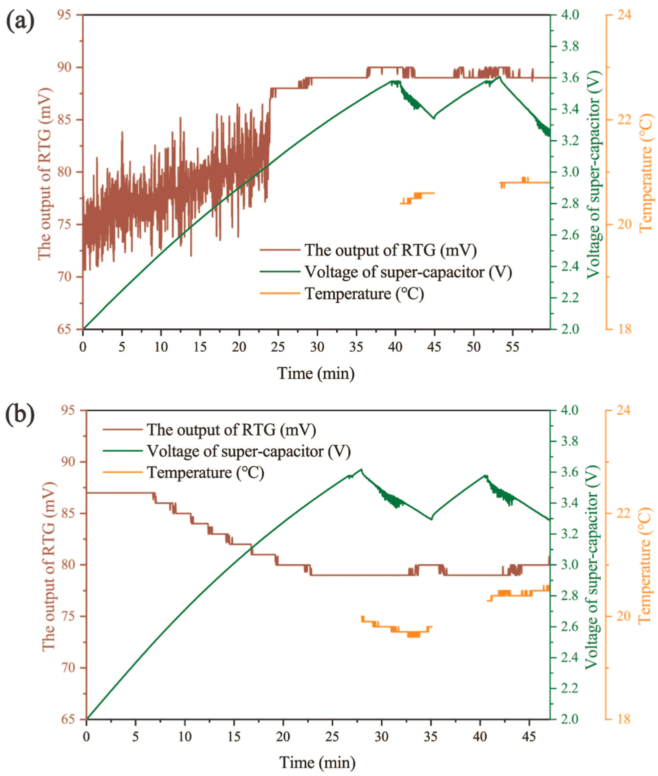

Fig. 7. Operational status of WSN node (a) at the ocean surface and (b) in the underwater environment.

highly stable output due to the absence of factors such as sea breeze.

The performance of the WSN node varies in different environments, corresponding to the RTG output performance test results. In the underwater environment, the lead time, also known as the energy collection time before the sensor starts working, is shorter than that at the ocean surface. Therefore, the total time taken to complete two operational cycles is also short in the underwater environment.

3.3. Study of the WSN node operation stability

3.3.1. Impact of the RTG output

The RTG output largely determines the charging time of the supercapacitor and the operational time of the sensor in the self-powered WSN node system. Therefore, the RTG voltage input to the system was adjusted by changing the heat source power and other means during the experiment to explore further the operational performance of the WSN node system. Based on this approach, the operational status of the WSN node system was monitored. The operational curves of WSN node under different RTG output voltages are shown in Table 3.

During the operation of the WSN node, the charging speed of the supercapacitor increases with the increase in voltage generated by the RTG. For instance, completing a single charging process at a voltage of 107 mV takes less than 30 s, whereas completing a charging process at a voltage of 43 mV takes more than 170 s. Correspondingly, although the number of cycles during the test time is decreasing as the voltage is increased from 83 mV to 107 mV, the total sensor operating time increases from 621 s to 1408 s in 30 mins, an increase of about two times due to the increasing voltage generated by the RTG. And further details can be found in Fig. S7 of the Supplementary Material. The results of the tests indicate that the high RTG output voltage is required for prolonged continuous monitoring in marine areas. Conversely, low RTG output voltage is preferable for intermittent monitoring in marine areas. This can be achieved by reducing the number of the TE module.

3.3.2. Impact of variations in monitored data

The sensitivity of the WSN node in acquiring data during operation was tested to analyze the influence of variations in sensor monitoring data on the WSN node operation due to the temperature sensor used in this study. The surrounding temperature of the sensor was altered to verify its sensitivity. The environment of the RTG remained constant in the experiment to mitigate the influence of other related factors, with only the temperature surrounding the sensor being changed. The test results for the warming and cooling cases are shown in Fig. 8, showing that the assembled WSN node can detect temperature changes during operation.

The sensor's operating time within the WSN node system is 621 s in the warming environment and 622 s in the cooling environment. This finding indicates that variations in monitoring data do not have an impact on sensor's operating time these two values are very close. The

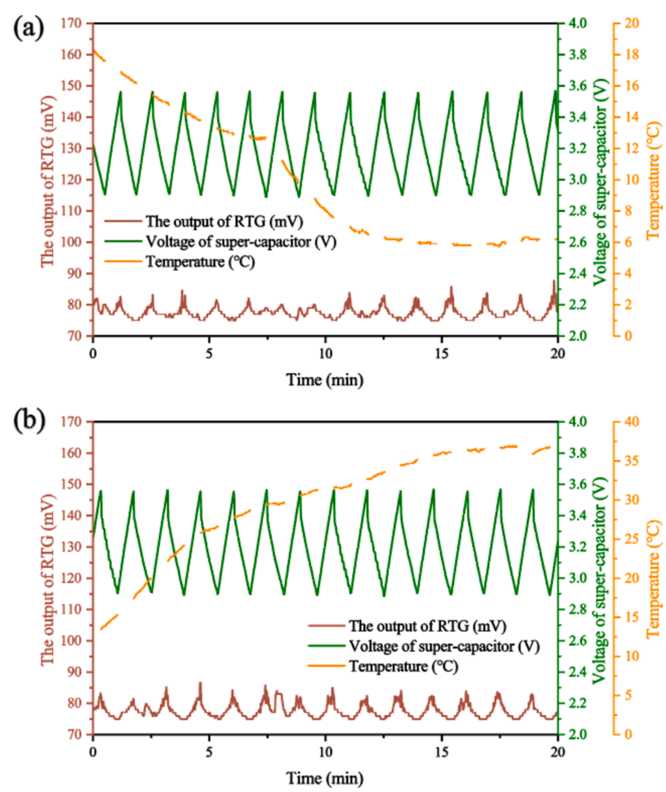

Fig. 8. Working status of WSN node under (a) warming and (b) cooling alternating temperature treatments.

Table 3
Working status of the WSN node under different RTG outputs.

The average output voltage of the RTG (mV)	Single charge time (s)	Single discharge time (s)	Total charge time (s)	Total discharge time (s)	The number of cycles (times)	The range of tested temperature (°C)
43	173	24	1584	216	9	18.8 ~ 20.1
83	62	33	1179	621	18	17.0 ~ 18.0
97	35	64	625	1175	17	17.9 ~ 19.2
107	28	97	392	1408	14	19.7 ~ 20.2

supercapacitors show good consistency with the same trend in the voltage fluctuation curves over the 13 cycles. The voltages at both ends of the RTG and the supercapacitor overlap almost identically in both environments. This finding suggests that the sensor's power consumption can remain consistent regardless of the changes in the testing environment. Although the voltage curve of the RTG still exhibits fluctuations, it does not affect the overall cycling of the system. It is enough to state that the differences in operation during warming and cooling are practically negligible. This finding further indicates the excellent stability of the power supply in the self-powered WSN node system. The assembled WSN node system exhibits good detection sensitivity, and the variations in the monitored data do not affect the operational stability of the WSN node system.

3.3.3. Impact of distance

The nodes in WSN nodes are interconnected through wireless communication, and the reliability and quality of data transmission are crucial. Therefore, tests were conducted in this section to investigate the influence of data transmission distance on sensor operation. The results can provide insights into the energy consumption of nodes at different distances and whether data transmission is affected.

The self-powered WSN node system was kept stationary during the experiment to prevent variations in the results due to environmental changes. Moreover, the position of the data receiving end was altered. Four distances were tested: 1.8, 10.8, 16.8, and 27.0 m. Only the charging and discharging time of the WSN node was monitored to show the power consumption. The working status of WSN node at the different signal transmission distances is illustrated in Fig. 9. During the testing period, the WSN node system completed six full operational cycles. As the distance between the transmitter and receiver of the WSN node increased from closer to farther, the single working time of the temperature sensor, which is also the single discharge time, were recorded as 263, 264, 269, and 263 s, respectively. The four working times are nearly equal. Any slight fluctuations observed may be attributed to temperature variations in the WSN node environment. The voltage variation curves of the supercapacitor for six cycles remain relatively stable, demonstrating good consistency. This also means that the total working time of the temperature sensors at different distances between the transmitter and receiver of the WSN node is close to each other during the tests. This finding indicates that the power consumption of the sensor remains consistent within a certain transmission distance. This characteristic is beneficial for extending the lifespan of WSN node operations. This information can be utilized to optimize energy management strategies, prolong node lifespans, and enhance the reliability and quality of data transmission when WSN nodes are deployed on a large scale in the future.

4. Conclusion

In this study, the RTG was used as the power source of WSN node, and a self-powered WSN node system was successfully applied to ocean temperature monitoring by combining energy harvesting circuits and a sensor node. The whole system outputs the power generated by RTG without any other power input. Moreover, the problems of short operation time and environmental pollution of WSN node can be solved because of the long service life and high reliability of RTG. The cylindrical heat sources offer advantages such as compact structure and uniform surface temperature distribution. At a heat source power of 15 W, the RTG achieved P_{max} of 341.3 μW, V_{oc} of 113.8 mV, and I_{sc} of 12.6 mA. In underwater environments, the RTG exhibited a P_{max} of 2326.6 μW, V_{oc} of 376 mV, and I_{sc} of 28.2 mA. The effects of multiple factors on the operational stability of WSN node demonstrate the stable and

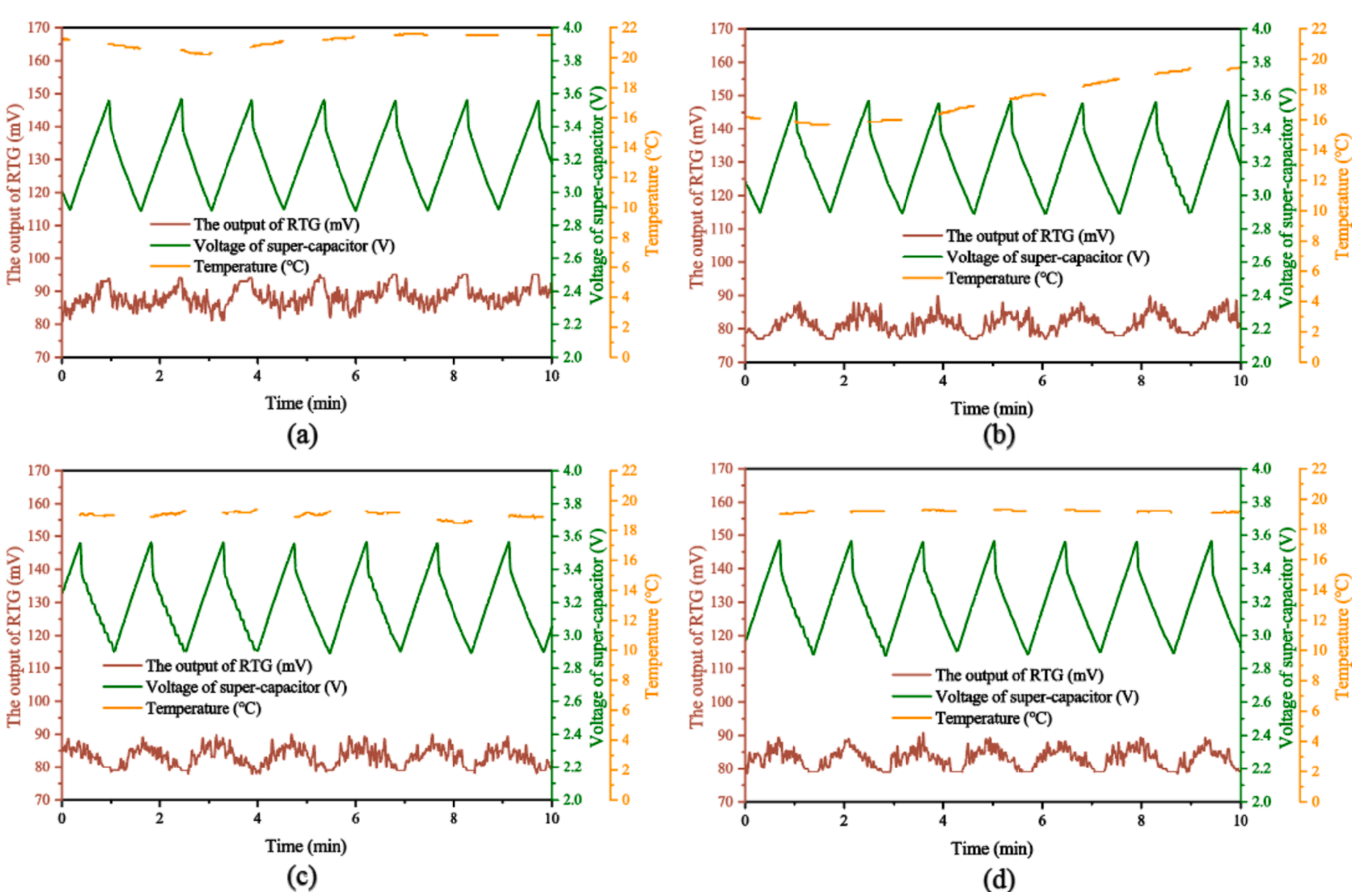

Fig. 9. Working status of WSN node when the distance between the transmitter and the receiver is (a) 1.8 m, (b) 10.8 m, (c) 16.8 m, and (d) 27 m.

continuous operation of the WSN node at the ocean surface and in underwater environments, with the RTG output underwater exhibiting superior performance. Correspondingly, the charging time for the WSN node is short underwater, allowing for long operational times within a given period. The self-powered WSN node exhibits stability, unaffected by changes in sensor environmental temperature and data transmission distance.

This work extends the application areas of RTG and has great potential for applications in the field of energy harvesting and reuse. The designed TE module can effectively fit into other irregularly shaped heat sources, such as the human body, automobile exhaust ducts, chimneys, and industrial heat pipes. The waste heat generated can be recovered to power other electronic devices in various fields.

CRediT authorship contribution statement

Chao Chen: Writing – review & editing, Writing – original draft, Supervision, Methodology, Formal analysis, Data curation, Conceptualization. **Chen Wang:** Writing – review & editing, Methodology, Funding acquisition, Conceptualization. **Zhiheng Xu:** Writing – review & editing, Formal analysis, Conceptualization, Funding acquisition. **Mingxin Bian:** Writing – review & editing, Methodology. **Hongyang Jia:** Writing – review & editing, Methodology. **Ting Cai:** Writing – review & editing. **Yunpeng Liu:** Writing – review & editing, Funding acquisition. **Xiaobin Tang:** Writing – review & editing, Methodology.

Declaration of competing interest

The authors declare that they have no known competing financial interests or personal relationships that could have appeared to influence the work reported in this paper.

Acknowledgements

This research was supported by the National Natural Science Foundation of China (Grant Nos. 12275132 and 12075119), the Fundamental Research Funds for the Central Universities (Grant No. NT2023013), and the prospective layout project of Nanjing University of Aeronautics and Astronautics (Grant No. ILB240161A24).

Appendix A. Supplementary data

Supplementary data to this article can be found online at https://doi.org/10.1016/j.applthermaleng.2024.124746.

Data availability

Data will be made available on request.

References

[1] S. Gorjian, F. Calise, K. Kant, M.S. Ahamed, B. Copertaro, G. Najafi, X. Zhang, M. Aghaei, R.R. Shamshiri, A review on opportunities for implementation of solar energy technologies in agricultural greenhouses, J. Clean. Prod. 285 (2021) 124807, https://doi.org/10.1016/j.jclepro.2020.124807.
[2] B. Dai, Q. Wang, S. Liu, D. Wang, L. Yu, X. Li, Y. Wang, Novel configuration of dual-temperature condensation and dual-temperature evaporation high-temperature heat pump system: Carbon footprint, energy consumption, and financial assessment, Energ. Conver. Manage. 292 (2023) 117360, https://doi.org/10.1016/j.enconman.2023.117360.
[3] R. Rayner, C. Jolly, C. Gouldman, Ocean observing and the blue economy, Front. Mar. Sci. 6 (2019) 330, https://doi.org/10.3389/fmars.2019.00330.
[4] B. Dai, H. Qi, S. Liu, Z. Zhong, H. Li, M. Song, M. Ma, Z. Sun, Environmental and economical analyses of transcritical CO_2 heat pump combined with direct dedicated mechanical subcooling (DMS) for space heating in China, Energ. Conver. Manage. 198 (2019) 111317, https://doi.org/10.1016/j.enconman.2019.01.119.
[5] T.B. Rudolph, M. Ruckelshaus, M. Swilling, E.H. Allison, H. Osterblom, S. Gelcich, P. Mbatha, A transition to sustainable ocean governance, Nature Communication. 11 (2020) 3600, https://doi.org/10.1038/s41467-020-17410-2.
[6] T. Kageyama, M. Miura, A. Maeda, A. Mori, S.S. Lee. A wireless sensor network platform for water quality monitoring. Sensors. (2016) 1–3. https://ieeexplore.ieee.org/document/7808887 (accessed May 15, 2024).
[7] L.G. Fang, Z.B. Liu, H.L. Li, C.D. Gu, M.L. Dai, Application of wireless sensor network for m2m in precision fruits, Adv. Mat. Res. 267 (2011) 482–487, https://doi.org/10.4028/www.scientific.net/AMR.267.482.
[8] A. Cilfone, L. Davoli, L. Belli, G. Ferrari, Wireless mesh networking: an IoT-oriented perspective survey on relevant technologies, Future Internet. 11 (2019) 99, https://doi.org/10.3390/fi11040099.
[9] B. Rashid, M.H. Rehmani, Applications of wireless sensor networks for urban areas: A survey, J. Netw. Comput. Appl. 60 (2016) 192–219, https://doi.org/10.1016/j.jnca.2015.09.008.
[10] A. Ali, A. Khelil, F.K. Shaikh, N. Suri, Efficient predictive monitoring of wireless sensor networks, Int. J. Autonomous Adaptive Commun. Syst. 5 (2012) 233–254, https://doi.org/10.1504/IJAACS.2012.047657.
[11] L. Belli, A. Cilfone, L. Davoli, G. Ferrari, P. Adorni, F. Di Nocera, A. Dall'Olio, CPellegrini, M. Mordacci, E. Bertolotti, IoT-Enabled smart sustainable cities: challenges and approaches, Smart Cities 3 (2020) 1039–1071, https://doi.org/10.3390/smartcities3030052.
[12] A. Shahanaghi, Y. Yang, R.M. Buehrer, On the stochastic link modeling of static wireless sensor networks in ocean environments, Conference on Computer Communications. (2019) 1144–1152. doi: 10.1109/INFOCOM.2019.8737530.
[13] V. Garrido-Momparler, M. Peris, Smart sensors in environmental/water quality monitoring using IoT and cloud services, Trends Environ. Anal. Chem. 35 (2022) e00173.
[14] G. Verma, V. Sharma, A novel thermoelectric energy harvester for wireless sensor network application, Transactions on Industrial, Electronics 66 (2019) 3530–3538, https://doi.org/10.1109/TIE.2018.2863190.
[15] K. Yamashita, S.M. Villanueva, Integration of renewable energy sources, energy storages, and their impacts, Encyclopedia Electr. Electronic Power Eng. (2023) 36–44, https://doi.org/10.1016/B978-0-12-821204-2.00130-6.
[16] S. Lineykin, M. Sitbon, A. Kuperman, Design and optimization of low-temperature gradient thermoelectric harvester for wireless sensor network node on water pipelines, Appl. Energy 283 (2021) 116240, https://doi.org/10.1016/j.apenergy.2020.116240.
[17] M. Babar, A. Rahman, F. Arif, G. Jeon, Energy-harvesting based on internet of things and big data analytics for smart health monitoring, Sustainable Comput. Inf. Syst. 20 (2018) 155–164, https://doi.org/10.1016/j.suscom.2017.10.009.
[18] M.R. Sarker, A. Riaz, M.S.H. Lipu, M.H. Md Saad, M.N. Ahmad, R.A. Kadir, J. L. Olazagoitia, Micro energy harvesting for IoT platform: Review analysis toward future research opportunities, Heliyon. 10 (2024) e27778.
[19] Z. Yuan, X. Tang, Y. Liu, Z. Xu, K. Liu, Z. Zhang, W. Chen, J. Li, A stacked and miniaturized radioisotope thermoelectric generator by screen printing, Sens. Actuators, A 267 (2017) 496–504, https://doi.org/10.1016/j.sna.2017.10.055.
[20] K. Liu, Y. Liu, Z. Xu, Z. Zhang, Z. Yuan, X. Guo, Z. Jin, X. Tang, Experimental prototype and simulation optimization of micro-radial milliwatt-power radioisotope thermoelectric generator, Appl. Therm. Eng. 125 (2017) 425–431, https://doi.org/10.1016/j.applthermaleng.2017.07.022.
[21] K. Liu, X. Tang, Y. Liu, Z. Xu, Z. Yuan, J. Li, Preparation and optimization of miniaturized radioisotope thermoelectric generator based on concentric filament architecture, J. Power Sources 407 (2018) 14–22, https://doi.org/10.1016/j.jpowsour.2018.10.052.
[22] L. Yang, Z.-G. Chen, M.S. Dargusch, J. Zou, High performance thermoelectric materials: progress and their applications, Adv. Energy Mater. 8 (2018) 1701797. https://onlinelibrary.wiley.com/doi/full/10.1002.
[23] X. Wang, R. Liang, P. Fisher, W. Chan, J. Xu, Critical design features of thermal-based radioisotope generators: A review of the power solution for polar regions and space, Renew. Sustain. Energy Rev. 119 (2020) 109572, https://doi.org/10.1016/j.rser.2019.109572.
[24] X. Wang, J. Qi, W. Deng, G. Li, X. Gao, L. He, S. Zhang, An optimized design approach concerning thermoelectric generators with frustum-shaped legs based on three-dimensional multiphysics model, Energy 233 (2021) 120810, https://doi.org/10.1016/j.energy.2021.120810.
[25] K. Liu, X. Tang, Y. Liu, Z. Xu, Z. Yuan, Z. Zhang, Enhancing the performance of fully-scaled structure-adjustable 3D thermoelectric devices based on cold–press sintering and molding, Energy 206 (2020) 118096, https://doi.org/10.1016/j.energy.2020.118096.
[26] K. Liu, X. Tang, Y. Liu, Z. Xu, Z. Yuan, D. Ji, S. Ramakrishna, Experimental optimization of small–scale structure–adjustable radioisotope thermoelectric generators, Appl. Energy 280 (2020) 115907, https://doi.org/10.1016/j.apenergy.2020.115907.
[27] Z. Yuan, X. Tang, Y. Liu, Z. Xu, K. Liu, J. Li, Z. Zhang, H. Wang, Improving the performance of a screen-printed micro-radioisotope thermoelectric generator through stacking integration, J. Power Sources 414 (2019) 509–516, https://doi.org/10.1016/j.jpowsour.2019.01.040.
[28] M. Bian, Z. Xu, C. Meng, H. Zhao, X. Tang, Novel geometric design of thermoelectric leg based on 3D printing for radioisotope thermoelectric generator, Appl. Therm. Eng. 212 (2022) 118514, https://doi.org/10.1016/j.applthermaleng.2022.118514.
[29] F.K. Shaikh, S. Zeadally, Energy harvesting in wireless sensor networks: A comprehensive review, Renew. Sustain. Energy Rev. 55 (2016) 1041–1054, https://doi.org/10.1016/j.rser.2015.11.010.
[30] J. Qi, X. Wang, D. Yang, G. Li, Feasibility study on radioisotope-powered thermophotovoltaic/thermoelectric hybrid power generation system used in deep-sea: From design to experiment, Appl. Energy 358 (2024) 122604, https://doi.org/10.1016/j.apenergy.2023.122604.

[31] Z. Xu, J. Li, X. Tang, Y. Liu, T. Jiang, Z. Yuan, K. Liu, Electrodeposition preparation and optimization of fan-shaped miniaturized radioisotope thermoelectric generator, Energy 194 (2020) 116873, https://doi.org/10.1016/j.energy.2019.116873.

[32] H. Wang, Z. Xu, C. Wang, Z. Hou, M. Bian, N. Zhuang, H. Tao, Y. Wang, X. Tang, Optimized design and application performance analysis of heat recovery hybrid system for radioisotope thermophotovoltaic based on thermoelectric heat dissipation, Appl. Energy 355 (2024) 122259, https://doi.org/10.1016/j.apenergy.2023.122259.

[33] R. Buchalik, G. Nowak, I. Nowak, Mathematical model of a thermoelectric system based on steady- and rapid-state measurements, Appl. Energy 293 (2021) 116943, https://doi.org/10.1016/j.apenergy.2021.116943.

[34] S. Kim, Analysis and modeling of effective temperature differences and electrical parameters of thermoelectric generators, Appl. Energy 102 (2013) 1458–1463, https://doi.org/10.1016/j.apenergy.2012.09.006.